Inorganic Chemistry

pubs.acs.org/IC Article

Structure, Stability, and Photocatalytic Activity of a Layered Perovskite Niobate after Flux-Mediated Sn(II) Exchange

Shaun O'Donnell, Avery Smith, Abigail Carbone, and Paul A. Maggard*

Cite This: *Inorg. Chem.* 2022, 61, 4062−4070

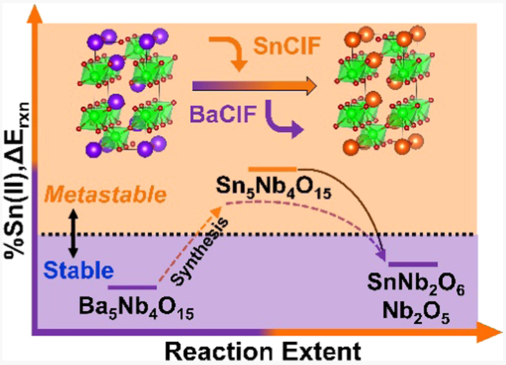

ABSTRACT: A new strategy to incorporate the Sn(II) cation and its stereoactive lone pair into the structure of a photocatalytic oxide has been achieved by leveraging the asymmetric coordination environments within the (111)-oriented perovskite-type layers of $Ba_5Nb_4O_{15}$. This layered perovskite represents one of the few known photocatalysts capable of efficiently splitting water, but its activity is restricted to ultraviolet radiation owing to its large band gap. By reacting this layered niobate at 350 °C for 24 h within a low-melting $SnCl_2/SnF_2$ salt, the new $(Ba_{1-x}Sn_x)Nb_4O_{15}$ ($x = 0$−0.5; $P\bar{3}m1$; $a = 5.79650(5)$ Å, $c = 11.79288(8)$ Å; $Z = 2$) has been prepared in high purity with up to ~50% Sn(II) cations. Statistical disordering of the Sn(II) cations was probed by neutron diffraction Rietveld refinements and found to occur predominantly over the asymmetric cation sites, Ba2 and Ba3, for the 40% Sn(II) composition of $x = 0.4$. An increasing Sn(II) amount significantly red-shifts the band gap (E_g) from 0% Sn for $x = 0$ (3.78 eV; ultraviolet, indirect) to 40% Sn for $x = 0.4$ ($E_g = 2.35$ eV; visible, indirect), as found by UV−vis diffuse reflectance. Density functional theory calculations show an increasing metastability, i.e., a thermodynamic instability toward decomposition to the simpler oxides SnO, Nb_2O_5, and $SnNb_2O_6$. A synthetic limit of ~50% Sn(II) cations can be kinetically stabilized under these reaction conditions. For the highest Sn(II) amounts, photocatalytic rates are observed for the production of molecular oxygen from water of up to ~77 μmol O_2 h^{-1} g^{-1} (visible irradiation) and ~159 μmol O_2 h^{-1} g^{-1} (UV−vis irradiation), with apparent quantum yields of ~0.35 and 0.52%, respectively. By comparison, pure $Ba_5Nb_4O_{15}$ exhibits no measurable photocatalytic activity under visible-light irradiation. Electronic structure calculations show that the decreased band gap stems from the introduction of the Sn(II) cations and the formation of a higher-energy valence band arising from the filled $5s^2$ valence orbitals. Thus, visible-light bandgap excitation occurs from electronic transitions predominantly involving the Sn(II) ($5s^2$) to Nb(V) ($4d^0$) cations. This study demonstrates the new and powerful utility of low-temperature Sn(II)-exchange reactions to sensitize layer-type oxide photocatalysts to the visible region of the solar spectrum, which is facilitated by exploiting their asymmetric cation environments.

I. INTRODUCTION

For the conversion of sunlight to chemical fuels, layered perovskite oxides represent some of the most efficient semiconducting photocatalysts for the reduction and oxidation of water.[1−4] This includes all known variations in the crystallographic orientations of perovskite-type layers, such as the (100) orientation in the Dion−Jacobson-type $KA_2Nb_3O_{10}$ (A = Ca, Sr) and $A'LaM_2O_7$ (A′ = K, Rb, Cs; M = Nb, Ta),[5−7] the (110) orientation in $La_2Ti_2O_7$ and $Sr_2M_2O_7$ (M = Nb, Ta),[8−10] and the (111) orientation in $Ba_5M_4O_{15}$ and $BaLa_4Ti_4O_{15}$.[11−13] These are but a few examples among many that show high photocatalytic rates for H_2 and/or O_2 evolution under ultraviolet irradiation, with quantum yields approaching ~10−20%. In a few examples, including $Sr_2Ta_2O_7$ and $Ba_5Nb_4O_{15}$,[8,11] photocatalytic activity for overall water splitting has also been reported. However, their large band gaps, typically >3.4 eV (λ < 360 nm), restrict their photocatalytic activities to the smaller ultraviolet component of the solar spectrum.

More recent research efforts have focused on the sensitization of layered types of perovskite oxides to the visible-light wavelengths, such as via the surface attachment of Ru(II)-based molecular sensitizers[14,15] or the incorporation of late transition-metal cations such as Cu(I) or Ag(I).[16−19] Alternatively, a growing strategy has been the synthesis of Sn(II)-containing oxides that can typically exhibit much smaller band gaps of ~1.5−2.5 eV,[20−23] such as for the layered SnM_2O_6 (M = Nb, Ta) or Sn_2TiO_4 semiconductors.[24,25] While these semiconductors have shown promising visible-light photocatalytic rates for water oxidation and

Received: December 10, 2021
Published: February 22, 2022

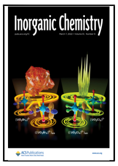

https://doi.org/10.1021/acs.inorgchem.1c03846

reduction, a relative paucity of Sn(II)-containing oxides is currently known and can be synthesized. This limitation is caused by the oxidation (in air) or disproportionation (in vacuum) of most Sn(II) oxides, such as starting at only ∼250 °C for SnO.[26,27] Further, many Sn(II)-containing perovskites are metastable with respect to decomposition to the simpler oxides, such as for perovskite-type "$SnZrO_3$" and "$SnHfO_3$". Recent synthetic approaches have demonstrated that low-melting salts can be utilized to prepare metastable oxides with the incorporation of the Sn(II) cation and thus helping to circumvent these limitations.[28−30] In this new approach, Sn(II)-containing oxides are formed as a result of the energetic offset provided by the co-formation of thermodynamically stable salts,[30] e.g., $BaHfO_3 + xSnCl_2 \rightarrow (Ba_{1-x}Sn_x)HfO_3 + xBaCl_2$. While these flux-mediated transformations have yielded smaller band gaps by ∼1−1.5 eV, the demonstrated scope of this synthetic approach has remained relatively limited.

Prior synthetic studies have not yet considered the impact of asymmetric cation sites on the ability to flux-exchange Sn(II) cations into the host crystalline structures. Presented herein are the results of the first such study, as performed by flux-mediated Sn(II)-exchange reactions with the (111)-layered perovskite $Ba_5Nb_4O_{15}$. The reaction products, $(Ba_{1-x}Sn_x)Nb_4O_{15}$ ($x = 0-0.5$), were characterized for the maximal extent of Sn(II) incorporation and for the crystallographic-site preferences by Rietveld refinements. Total energy calculations using density functional theory were utilized to determine the degree of metastability, i.e., with respect to decomposition to the simpler oxides, that accompanies the increasing Sn(II) substitution during the reaction. Electronic structure calculations reveal the occurrence of the stereoactive lone pairs expressed within the asymmetric cation sites of the layered structure. Concomitantly, the band gap of the Sn(II)-containing semiconductor is significantly decreased to ∼2.35 eV and exhibits a new visible-light photocatalytic activity for O_2 production in aqueous suspensions.

II. EXPERIMENTAL SECTION

II.I. Synthetic Procedure. Preparation of the $Ba_5Nb_4O_{15}$ precursor was adapted from previous literature methods.[12] Stoichiometric amounts of $BaCO_3$ (Alfa Aesar, 99.8%) and Nb_2O_5 (Alfa Aesar, 99.9985%) were first ground together for approximately 20 min using a mortar and pestle. The resulting mixture was placed into an alumina crucible and heated in a box furnace. The furnace was heated to 1100 °C at a rate of 12 °C min^{-1}, held for 36 h, and then allowed to radiatively cool to room temperature.

To prepare the Sn(II)-exchanged $(Ba_{1-x}Sn_x)_5Nb_4O_{15}$, the $Ba_5Nb_4O_{15}$ precursor was ground with the appropriate stoichiometric amounts of $SnCl_2$ (Alfa Aesar, 99% min) and SnF_2 (Alfa Aesar, 97.5%) (1:1 molar ratio) in a glovebox under an Ar atmosphere. The resulting mixture was transferred to a fused silica tube and sealed under a dynamic vacuum. The evacuated and flame-sealed tubes were placed into a box furnace and heated to 350 °C at a rate of 10 °C min^{-1}. The powders were held at 350 °C for 24 h and then were allowed to radiatively cool to room temperature inside the furnace. The products were washed multiple times and centrifuged with deionized water to remove any unreacted flux and BaClF side product. The product was then dried at 80 °C overnight.

II.II. Characterization Techniques. Powder diffractograms for all samples were collected on a Rigaku R-Axis Spider using Cu Kα radiation ($\lambda = 1.54056$ Å) from a sealed tube X-ray source (40 kV, 36 mA) and a curved image-plate detector. Neutron diffraction data were collected on a sample nominally loaded as $(Ba_{0.6}Sn_{0.4})Nb_4O_{15}$ (i.e., 40% Sn(II) cations) on the POWGEN (Beamline 11-A) time-of-flight (TOF) diffractometer at the Spallation Neutron Source (SNS) at Oak Ridge National Laboratory during cycle run 2019-B. Approximately 2 g of the sample was sealed in a cylindrical vanadium can and the data were collected at 298 K. A neutron beam with a wavelength of 1.5 Å at 60 Hz was used with a detector ∼2.0−4.7 m away from the sample. The crystal structure was refined by the Rietveld method using the GSAS-II software package.[31]

A JEOL SEM 6010LA scanning electron microscope operating with a 20 kV accelerating voltage along with a secondary electron imaging detector and a JEOL EDS silicon drift detector was used to collect SEM images and energy-dispersive X-ray spectra (EDS) for elemental analyses. A Shimadzu UV-3600 equipped with an integrating sphere was used to collect UV−vis diffuse reflectance spectra for all samples. A background was taken using a pressed barium sulfate disc. The data were transformed using the function, $F(R) = (1 - R_\infty)^2/(2R_\infty)$,[32,33] where R is the diffuse reflectance based on the Kubelka−Munk theory of diffuse reflectance. As $F(R)$ is equal to k/s, where k and s are the absorption and scattering coefficients, the band gaps can be extracted via Tauc plots of $(F(R) \times h\nu)^n$ versus photon energy for the allowed direct ($n = 2$) and indirect ($n = 1/2$) transitions. The direct and indirect transition energies were determined by extrapolating the linear portion of the Tauc plots to the baseline fit.

II.III. Photocatalysis Measurements. Four compositions were tested to probe the relationship between the extent of Sn(II) substitution in $(Ba_{1-x}Sn_x)_5Nb_4O_{15}$ and its photocatalytic activity. These compositions included samples with 0, 10, 30, or 50% Sn(II)-exchange, which were prepared in high purity according to powder XRD. The activity at each composition was measured in four separate runs and samples under identical conditions, according to previously reported procedures.[33,34] To begin, ∼100 mg of each sample was placed into a fused silica reaction cell containing either 0.05 M $AgNO_3$ or 0.05 M $Na_2S_2O_8$ as a sacrificial oxidant, followed by degassing via sonication and purging with flowing N_2 gas. The particles were kept suspended with stirring, and the reaction cell was irradiated with a photon flux of ∼200 mW cm^{-2} from a high-pressure Xenon arc lamp. Infrared and ultraviolet light-cutoff filters were attached to the arc lamp window to irradiate the particles under combined ultraviolet−visible light ($\lambda > 230$ nm) or only visible light ($\lambda > 400$ nm). The photocatalytic activity of each sample was measured twice under ultraviolet−visible light and twice under visible light. The photocatalytic production of O_2 from water in each run was measured volumetrically using a sliding liquid bubble in a horizontal tube. Rate measurements were taken every 10 min for 90 min and then every 30 min afterward. The gas product was characterized as O_2 using a gas chromatograph. No surface-attached cocatalysts were employed for the photocatalytic measurements, and thus, rates are obtained that are representative of the bare particles' surfaces. The samples did not show any detectable photocatalytic activity for H_2 production using a 1 wt % Pt cocatalyst in an aqueous H_2PtCl_6 solution.

II.IV. Electronic Structure and Total Energy Calculations. Total energy and electronic structure calculations were performed using density functional theory methods, as implemented in the Vienna ab initio simulation package (VASP; ver. 4.6).[35,36] To model the chemical compositions with 20 and 40% Sn(II) cations, a superstructure was created with dimensions 2 × 2 × 2 of the original $Ba_5Nb_4O_{15}$ unit cell (space group: $P\bar{3}m1$). The superstructure contained a total of 40 Ba sites, of which 20% and 40% were randomly replaced with Sn(II) cations, giving the respective compositions of $Ba_4SnNb_4O_{15}$ and $Ba_{24}Sn_{16}Nb_{32}O_{150}$. The full Sn(II)-substituted structure was also created with the composition $Sn_5Nb_4O_{15}$, with the complete replacement of the Ba cations with Sn(II) cations. Calculations employed Perdew−Burke−Ernzerhof functionals in the generalized gradient approximation using the projector augmented wave method.[37] The Brillouin zone was automatically sampled using a 4 × 4 × 2 Monkhorst−Pack grid. Full geometry relaxation of the unit cell and all atomic positions were performed with energy and ionic-step convergence criteria set at 10^{-6} and 10^{-2}, respectively.

Total internal energy calculations were utilized to calculate the stability of the Sn(II)-containing compositions against decomposition to the simpler oxides, e.g., SnO and $SnNb_2O_6$, according to procedures established previously.[28,29,38,39] Prior studies on hundreds of oxides show a typical accuracy to within a standard deviation of ~24 meV atom^{-1} by this approach.[38] By this method, the decomposition enthalpies of the $(Ba_{1-x}Sn_x)_5Nb_4O_{15}$ compounds are estimated with respect to the simpler oxides according to the following phase relationships and eqs 1 and 2

$$(Ba_{1-x}Sn_x)_5Nb_4O_{15} \rightarrow (1-x)Ba_5Nb_4O_{15} + 5xSnO + 2xNb_2O_5 \quad (x < 0.4) \tag{1}$$

$$(Ba_{1-x}Sn_x)_5Nb_4O_{15} \rightarrow (1-x)Ba_5Nb_4O_{15} + 3xSnO + 2xSnNb_2O_6 \quad (x \geq 0.4) \tag{2}$$

For example, for $x = 0.4$, or 40% Sn(II) cations, the balanced decomposition is given by eq 3

$$(Ba_{0.6}Sn_{0.4})_5Nb_4O_{15} \rightarrow 0.6Ba_5Nb_4O_{15} + 1.2SnO + 0.8SnNb_2O_6 \tag{3}$$

The decomposition of the Sn(II)-containing layered perovskite is modeled to yield the known thermodynamically stable oxide products, in which the entropic terms are considered negligible and thus $\Delta_{rxn}G \approx \Delta_{rxn}H$. The formation energies of the metal oxides were benchmarked for consistency against values found in the open quantum materials database (OQMD),[40] as determined by total energy calculations within VASP at 0 K.

III. RESULTS AND DISCUSSION

III.I. Synthesis and Structural Characterization. The barium niobate with a layered perovskite-type structure, $Ba_5Nb_4O_{15}$, was synthesized using traditional high-temperature conditions with the known structure shown in Figure 1. Lattice parameter refinements of the powder XRD data yielded a = 5.8083(6) Å and c = 11.8176(6) Å, consistent with prior literature reports.[11,12] Briefly, the structure crystallizes in a hexagonal space group (No. 164; $P\bar{3}m1$) and can be described as containing slabs of perovskite layers in the (111) crystallographic orientation with a corresponding thickness of four octahedra. These consist of two symmetry-unique NbO_6 octahedra and three symmetry-unique Ba sites. The intralayer versus interlayer Ba sites have a molar ratio of 3:2, with two of the sites (Ba1 and Ba3) located in the (111) perovskite layers with a combined multiplicity of 3 and the Ba2 site located between the layers with a multiplicity of 2. This layered $Ba_5Nb_4O_{15}$ perovskite was next reacted within a peritectic SnClF flux (mp ~ 195 °C) at stoichiometric loading increments of 10%, i.e., $(Ba_{1-x}Sn_x)Nb_4O_{15}$ from x = 0.1 to 1.0, and thus targeting up to 100% Sn(II) exchange of the Ba cations, i.e., potentially reaching "$Sn_5Nb_4O_{15}$". The representative chemical reaction is given by eq 4

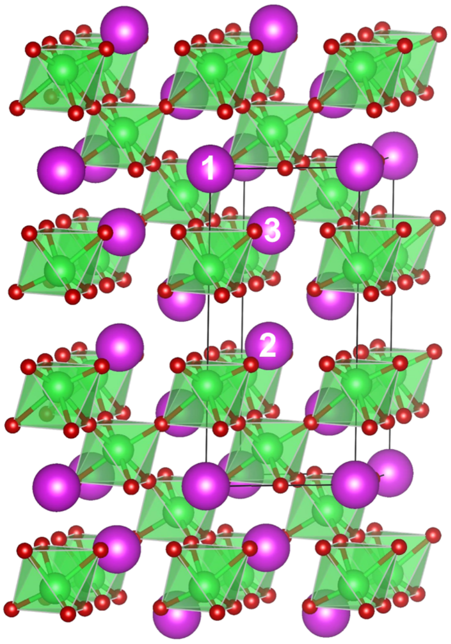

Figure 1. Polyhedral view of the crystal structure of $Ba_5Nb_4O_{15}$ down the [100] direction, with the unit cell outlined and the atom types labeled.

$$Ba_5Nb_4O_{15} + 5xSnClF \rightarrow (Ba_{1-x}Sn_x)_5Nb_4O_{15} + 5xBaClF \tag{4}$$

The SnClF salt melts at only ~195 °C and enables the reaction to occur at relatively low temperatures, as limited by the chemical diffusion of the divalent cations in the layered perovskite. The formation of the BaClF salt from the SnClF reactant provides a substantial thermodynamic driving force of approximately −1028 kJ mol^{-1}, as described previously in detail in prior studies.[24,28]

After dissolving and washing away the BaClF side product in each reaction, powder XRD data were taken on all $(Ba_{1-x}Sn_x)Nb_4O_{15}$ samples, as plotted in Figure S1 in the Supporting Information. These data show the maintenance of the layered perovskite-type structure with increasing Sn(II) exchange and the appearance of a $Sn_2Nb_2O_7$ impurity at the highest concentrations of 60−100% Sn(II). With the higher Sn(II) reaction loading, energy-dispersive spectroscopy (EDS) data showed a decreasing amount of Ba and an increasing amount of Sn, listed in Table S1 and Figure S2 in the Supporting Information. For samples loaded at 20% and 40% Sn(II) exchanges, experimental EDS data yielded percentages of ~23(2)% and ~44(3)%, respectively, together with a corresponding decrease in the mole fraction of barium. Elemental mapping showed that the distribution of Ba, Nb, and Sn was also relatively homogeneous throughout the sample (Figure S2), with a range of particle sizes and morphologies.

Rietveld refinements were carried out on high-resolution neutron diffraction data of the 40% Sn sample to probe the incorporation of the Sn(II) cation into the intralayer and interlayer Ba cation sites in the structure. Neutron diffraction was used for its higher sensitivity to the O atom positions and because of the similarities in the X-ray scattering factors of Ba and Sn. The starting structural model was that reported previously for $Ba_5Nb_4O_{15}$[11] but with the introduction of mixed Ba/Sn sites and occupancies. Results of the refinement (Figure 2) yielded slightly contracted lattice constants (a = 5.79650(5) Å and c = 11.79288(8) Å) consistent with the smaller Sn(II) cation and a refined composition of $Ba_{0.68}Sn_{0.32}Nb_4O_{15}$. The refined composition is slightly less than the loaded 40% Sn(II) cations and less than the 44% measured by EDS, but which is within standard deviation. Selected refinement parameters and atomic coordinates and occupancies are listed in Table S2.

Structure refinements reveal that the substitution of the Ba sites by Sn(II) cations occurs on the interlayer Ba2 (~52(3)% Sn) and intralayer Ba3 (~27(4)% Sn) positions, as compared to that on the intralayer Ba1 (~0.00(8)%) position. The Ba1 site is located in the middle of the perovskite layer and is likely

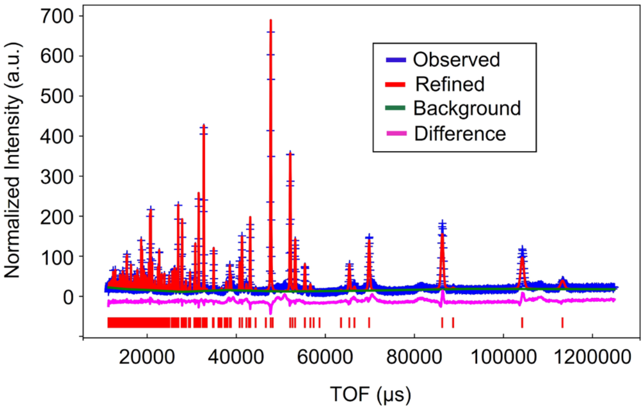

Figure 2. Plot of the Rietveld refinement results of the neutron diffraction data for $(Ba_{0.66}Sn_{0.32})_5Nb_4O_{15}$.

the most sterically restricted site for the Sn(II) cations to reach by ion diffusion (Figure 1). The local coordination environments of each of the three different Ba/Sn sites are shown together in Figure 3. While the 12-fold coordination of the Ba1/Sn1 site is relatively symmetric in terms of distances, the local coordination environments for the Ba2/Sn2 and Ba3/Sn3 sites are shown to be highly asymmetric along the *c*-axis direction. Each of the latter has three shorter and three longer distances to the symmetry-equivalent O atoms above and below, with the Ba2/Sn2 site significantly more asymmetric. Prior studies have shown that the Sn(II) cation should exhibit a strong stereoactive lone pair from its $5s^2$ electron configuration[41] and therefore may prefer crystallographic sites within the structure that can be host to a strongly distorted coordination environment. This is consistent with the refinements showing that the Sn(II) cations preferentially occupy the Ba2/Sn2 and Ba3/Sn3 sites. In addition, electronic calculations (described below) yield the lowest energies for Sn(II) substitution on the Ba2 and Ba3 sites and electron density plots showing lone pair formation. Thus, as compared to the recently reported Sn(II) substitution in the cubic perovskite structure,[28,29] containing a symmetric 12-fold coordination site, the layered (111) perovskite structure provides more favorable asymmetric coordination for occupation by the Sn(II) cations.

III.II. Metastability and Thermal Decomposition. As described previously, many ternary Sn(II)-oxides are thermodynamically metastable, such as with respect to other lower-energy polymorphs or more commonly toward decomposition to their constituent binary oxides. To date, there are only two known Sn(II)-niobates, $SnNb_2O_6$ and $Sn_2Nb_2O_7$, and only the former is calculated to be thermodynamically stable against decomposition to the binary oxides. As described previously for Sn(II)-containing perovskite oxides, total energy calculations via DFT methods were thus performed to probe the thermodynamic stability of the $(Ba_{1-x}Sn_x)_5Nb_4O_{15}$ solid solution as a function of the increasing Sn(II) content and synthesizability of up to 50% Sn(II) cations.

Total energy calculations of the geometry-relaxed structures for 20%, 40%, and 100% Sn(II) cations show an increasing metastability beginning at about 20% Sn(II) cations, as given by the decomposition reaction in eqs 1 and 2 (above). For 0% Sn(II) cations, the $Ba_5Nb_4O_{15}$ compound is stable against decomposition by +0.367 eV $atom^{-1}$, consistent with previously reported values in the online Materials Project Database.[40] By contrast, the fully Sn(II)-substituted composition of $Sn_5Nb_4O_{15}$ was calculated to be metastable with a calculated decomposition reaction energy (to SnO and $SnNb_2O_6$) of −0.066 eV $atom^{-1}$. The intermediate Sn(II) percentages were modeled by random substitutions of the Ba for Sn cations in a supercell approach. The total energy changes arising from Sn(II) substitution on the cation sites fell in the energetic order of Ba3 < Ba2 < Ba1. For example, the substitution of 20% Sn(II) cations on the Ba3 site was ∼260 meV $formula^{-1}$ (∼10.8 meV per Sn atom) lower in energy than for substitution on the Ba2 site and which was, in turn, ∼280 meV $formula^{-1}$ (∼11.7 meV per Sn atom) lower in energy than for substitution on the Ba1 site. These results are consistent with the preferential occupation of the Sn(II) cations on the asymmetric Sn2/Ba2 and Sn3/Ba3 sites found by Rietveld analysis. Though the 20% Sn(II) composition is already slightly metastable with respect to decomposition by up to ∼4−27 meV $atom^{-1}$, depending on the crystallographic sites of Sn(II) occupation, at the 40% Sn(II) composition the metastability climbs to ∼30−45 meV $atom^{-1}$. Thus, all $(Ba_{1-x}Sn_x)_5Nb_4O_{15}$ compositions at or beyond 20% Sn(II) are thermodynamically unstable, emphasizing the need for low reaction temperatures to enable a kinetic-trapping of Sn(II) compositions of up to 50%, as illustrated in Figure 4 (right).

The thermodynamic stability of Sn(II)-niobates occurring at intermediate compositions was calculated, e.g., for the known $Sn_2Nb_2O_7$ structure and the alternate $BaNb_4O_{11}$ structure type by replacement of the Ba for Sn(II) cations.[42] The results are plotted together with $(Ba_{1-x}Sn_x)Nb_4O_{15}$ in the metastability diagram constructed for the SnO−Nb_2O_5 system in Figure 4. The "$Sn_5Nb_4O_{15}$" composition is found to be the most metastable of all of the considered Sn(II)-niobates. Its window of synthesizability, in terms of the maximal Sn(II) amount being ∼50%, is found to be comparable to the calculated metastability of $Sn_2Nb_2O_7$. The latter is the only other metastable Sn(II)-niobate that has been reported to be synthesized.[43] However, it should be noted that $Sn_2Nb_2O_7$ is significantly more stable than "$Sn_5Nb_4O_{15}$". This helps to

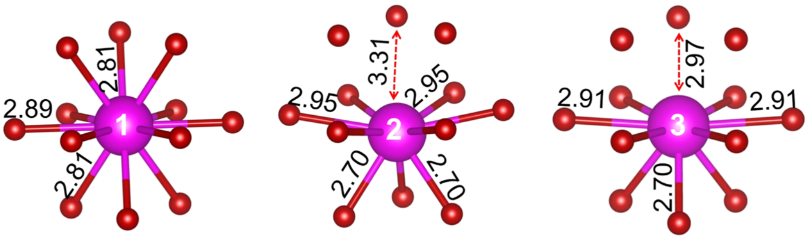

Figure 3. Local coordination environments of each of the three mixed Ba/Sn sites (purple) in $(Ba_{0.68}Sn_{0.32})_5Nb_4O_{15}$, with the interatomic distances to O (red) labeled in Å.

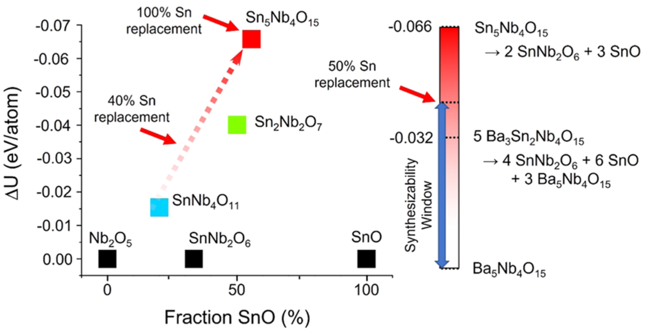

Figure 4. (Left) Calculated decomposition energies to simpler oxides for Sn(II)-niobates within the SnO−Nb_2O_5 phase space. The red, dashed arrow and scale bar on the right depict the change in ΔU as Sn(II) is substituted for Ba in $(Ba_{1-x}Sn_x)_5Nb_4O_{15}$, showing that the addition of Sn(II) cations results in a rapid increase in thermodynamic instability.

explain why synthetic attempts of $(Ba_{1-x}Sn_x)_5Nb_4O_{15}$ with more than 50% Sn(II) cations result in the appearance of $Sn_2Nb_2O_7$ (Figure S1 in the Supporting Information). When greater than ∼50% Sn(II) is reacted with $Ba_5Nb_4O_{15}$, the product becomes less thermodynamically stable than $Sn_2Nb_2O_7$ and results in the formation of $Sn_2Nb_2O_7$ rather than an increased substitution into $(Ba_{1-x}Sn_x)_5Nb_4O_{15}$. Also, given the similar Sn/Nb molar ratio of both Sn(II)-niobate compositions, the kinetic barrier to the reorganization of the ions is likely to be small. This suggests that it may be very difficult to reach the fully Sn(II)-substituted "$Sn_5Nb_4O_{15}$" composition unless a set of external conditions can be found which better stabilizes "$Sn_5Nb_4O_{15}$" as compared to $Sn_2Nb_2O_7$.

III.III. Optical and Photocatalytic Properties. The wide band gaps of layered perovskite oxides limit their potential practical utility with solar radiation, despite their high photocatalytic efficiencies for photocatalytic water splitting. For example, $Ba_5Nb_4O_{15}$ has been shown to split water into H_2 and O_2 with a quantum yield of ∼17%, but only using ultraviolet light at a wavelength of 270 nm because of its large band gap of 3.9 eV.[12] Addressing this limitation requires the introduction of new, higher-energy valence band states, which are possible in the relatively small class of known oxides containing Sn(II) cations. Prior studies have shown that the filled $5s^2$ orbital of the Sn(II) cation can interact with the filled O $2p^6$ states in the valence band, resulting in the formation of a higher-energy valence band comprised of Sn 5s/O 2p antibonding states.[41] This leads to smaller visible-light band gaps for many Sn(II)-oxides. Representative examples include $Sn_2Nb_2O_7$ (2.2 eV),[43] $SnTiO_3$ (1.9 eV),[44] and Sn_2TiO_4 (1.6 eV).[24] The role of Sn(II) substitution in decreasing the band gap and enabling the visible-light photocatalysis of $(Ba_{1-x}Sn_x)_5Nb_4O_{15}$ was therefore investigated.

UV−vis diffuse reflectance measurements were taken of $(Ba_{1-x}Sn_x)_5Nb_4O_{15}$ synthesized with 0%, 10%, 30%, and 50% Sn(II) cations. These data are shown as Tauc plots in Figure 5. The direct and indirect transition energies are extracted from the linear increases in absorption edges and are listed in Table 1. In all cases, the lowest-energy bandgap transition was found to be indirect and decreased with increasing Sn(II) substitution. The band gap of $Ba_5Nb_4O_{15}$ was measured to be ∼3.78 eV, consistent with prior reports.[11−13] With the substitution of only 10% Sn(II) cations, the band gap decreased most significantly to ∼2.37 eV, or a reduction of ∼1.4 eV. This band gap is now deeply within the visible-light energies, consistent with the yellowish color of its powder. Additionally, the direct transition substantially decreased from ∼3.90 to ∼2.78 eV. Further increases in the Sn(II) amount of up to 30 and 50% Sn(II) resulted in a smaller decrease in the band gaps down to ∼2.34 and ∼2.35 eV, respectively. A similar decrease is observed for the direct transition down to ∼2.69 eV. This trend clearly illustrates the beneficial role the substitution of Sn(II) can have on the visible-light absorption properties of layered metal oxides, which is a critical feature for any potential photocatalyst.

Table 1. Indirect and Direct Band Gap Transitions of $(Ba_{1-x}Sn_x)_5Nb_4O_{15}$

% Sn(II)	indirect (eV)	direct (eV)
0	3.78	3.90
10	2.37	2.78
30	2.34	2.69
50	2.35	2.69

To probe the origins of the reduced band gap of $(Ba_{1-x}Sn_x)_5Nb_4O_{15}$, electronic structure calculations were performed for representative Sn(II)-containing compositions, with the Sn(II) cations disordered over each of the three crystallographic sites. A representative densities-of-states (DOS) diagram is plotted in Figure 6 and overlaid with the individual atomic contributions. The conduction band states remain unchanged as compared to pure $Ba_5Nb_4O_{15}$ and are

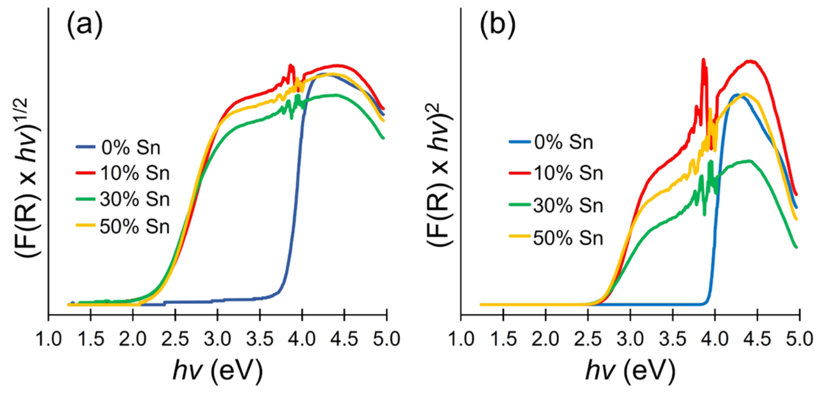

Figure 5. Tauc plots of UV−vis diffuse reflectance data for the (a) indirect transition and (b) direct transition of $(Ba_{1-x}Sn_x)_5Nb_4O_{15}$ compositions with 0−50% Sn(II) cations in 10% increments.

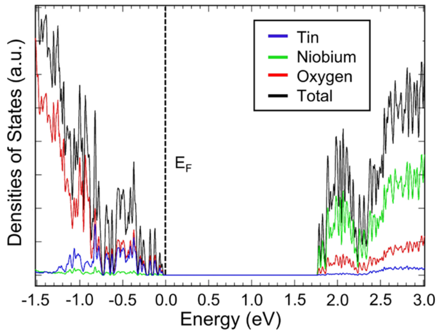

Figure 6. Plot of calculated DOS from density-functional theory for $(Ba_{0.6}Sn_{0.4})_5Nb_4O_{15}$, overlaid with the individual atomic orbital contributions and the Fermi level (dashed line).

comprised of primarily Nb 4d contributions mixed with minor amounts of O 2p contributions. An electron density contour map of the lowest ~0.5 eV edge of the conduction band is provided in Figure S3 (Supporting Information). This illustrates the delocalized electron density over the NbO_6 octahedra in the perovskite layer. Conversely, the topmost edge of the valence band within ~0.5 eV is formed from interactions between the Sn 5s and O 2p orbitals. A closer inspection shows that nearly all of the Sn(II)-cation contributions occur within the highest ~1.25 eV portion of the valence band edge, with the majority of the oxygen-based contributions displaced to relatively lower energies. The contributions of the Sn(II) cations to the valence band are shown within the electron density contour plot in Figure 7.

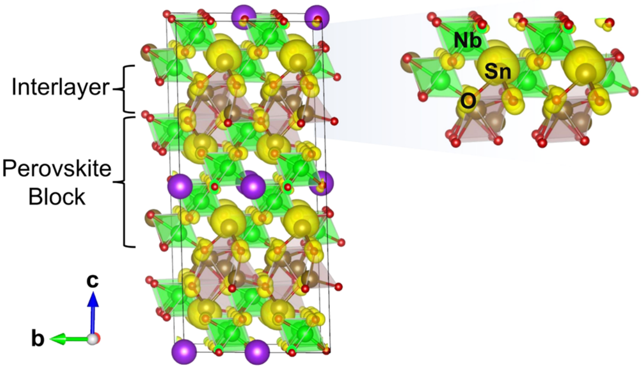

Figure 7. Electron density contour plot of the upper ~0.5 eV edge of the valence band for $(Ba_{0.6}Sn_{0.4})_5Nb_4O_{15}$, given in yellow shading. A zoomed-in region of the perovskite layer is projected out to the right, with each of the atom types labeled.

Within ~0.5 eV of the valence band edge, the electron density resides on those Sn(II) cations that are located within the perovskite layer. Furthermore, the stereoactive lone pair on the Sn(II) cation is clearly observed. As described in the Rietveld refinements, the stereoactive lone pair of the Sn(II) cation results in its energetic preference for the more asymmetric sites between the layers. The highest-energy electrons of the valence band edge are predominantly delocalized over the Sn(II) cations, mixed to a small extent with neighboring O 2p anions, which occur within the perovskite layer. The Sn(II) cations located between the perovskite layer contribute to the valence band at relatively lower energies, as expected for the asymmetric coordination environments that better accommodate their stereoactive lone pairs. This reveals the relationship between the asymmetric Sn(II) coordination environments that yield the lowest-energy valence band states (i.e., states deeper within the valence band rather than at the band edge) having the lowest-energy structures. Rietveld refinement shows that only a very small amount of the Sn(II) cations might be located within the perovskite layer at the higher-energy Ba1/Sn1 sites, meaning a smaller band gap may be possible in the future through a targeted Sn(II)-cation exchange at these sites as well.

Given the significantly reduced band gap of $(Ba_{1-x}Sn_x)_5Nb_4O_{15}$, the photocatalytic activities of the 0%, 10%, 30%, and 50% Sn(II) compositions were investigated under ultraviolet and visible lights for the photocatalytic oxidation of water to O_2. The photocatalytic data were measured according to previously established protocols[33,34] and without the use of any surface cocatalysts. An aqueous 0.05 M $AgNO_3$ solution was used as a sacrificial electron acceptor. As the reaction proceeds, the Ag(I) cations are reduced and deposited onto the particles' surfaces as Ag metal. As this slows the O_2 evolution over time, only the first 60 min was used to calculate the photocatalytic rates. All compositions were tested two times under combined ultraviolet−visible ($\lambda >$ 230 nm) or visible-light only ($\lambda >$ 400 nm) irradiation.

The photocatalysis data for the production of O_2 are plotted in Figure 8, and the rates are listed in Table 2. Under combined ultraviolet−visible irradiation, $Ba_5Nb_4O_{15}$ was highly active for water oxidation with a rate of ~68 μmol h^{-1} g^{-1}. However, it exhibited no activity under only visible-light irradiation. For $(Ba_{1-x}Sn_x)_5Nb_4O_{15}$ with 10% Sn(II) cations and a smaller band gap of ~2.37 eV, a significantly increased visible-light rate of ~59 μmol O_2 h^{-1} g^{-1} was measured (Figure 8b). Upon increasing the Sn(II) substitution to 30% and 50%, the visible-light photocatalytic rates increased moderately to ~77 and ~76 μmol O_2 h^{-1} g^{-1}. As the band gaps of the 10%, 30%, and 50% Sn(II) compositions are similar within ≤0.03

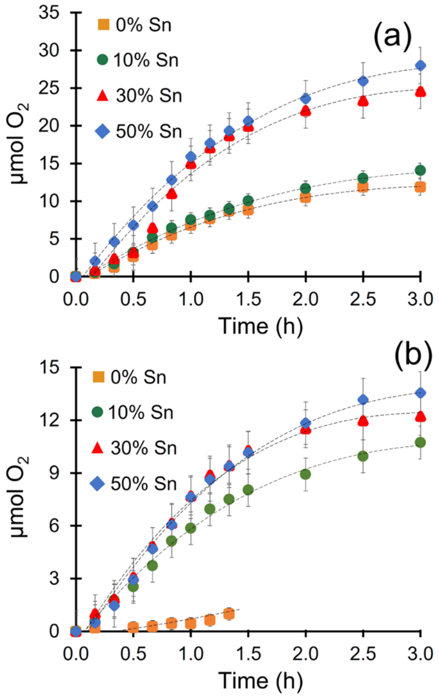

Figure 8. Plots of the photocatalytic activities of $(Ba_{1-x}Sn_x)_5Nb_4O_{15}$ for O_2 production under (a) UV + vis and (b) visible-only irradiation.

Table 2. Photocatalytic Rates of $(Ba_{1-x}Sn_x)Nb_4O_{15}$ for the Production of O_2 under Ultraviolet−Visible or Visible-Light-Only Irradiation

composition of $(Ba_{1-x}Sn_x)Nb_4O_{15}$	UV + vis [μmol O_2 h^{-1} g^{-1}]	visible [μmol O_2 h^{-1} g^{-1}]	% visible
0% Sn	67.9 ± 0.5		0
10% Sn	75.2 ± 4.1	58.6 ± 9.4	78
30% Sn	150.0 ± 1.2	76.9 ± 0.8	51
50% Sn	159.0 ± 1.2	76.2 ± 0.1	48

eV, the light absorption and therefore their photocatalytic activities are also relatively similar. The apparent quantum yield for O_2 production under visible-light only was determined to be ∼0.35% for the 30% and 50% Sn(II) compositions. These results clearly show that the substitution of Sn(II) into $Ba_5Nb_4O_{15}$ produces higher-energy valence band states, as arising from the $5s^2$-based Sn(II) cations, that are sufficient to drive water oxidation.

With the addition of ultraviolet irradiation, i.e., under both ultraviolet and visible lights, higher rates are generally observed for all Sn(II) compositions. Both the 10% Sn(II) composition and pure $Ba_5Nb_4O_{15}$ had relatively comparable rates of ∼75 μmol O_2 h^{-1} g^{-1}. It should be noted that $Ba_5Nb_4O_{15}$ is reported to achieve an apparent quantum yield of ∼17% under ultraviolet light.[12] For $(Ba_{1-x}Sn_x)_5Nb_4O_{15}$ with 30% and 50% Sn(II) cations, the photocatalytic rates are doubled to ∼150 and ∼159 μmol O_2 h^{-1} g^{-1}, respectively, with apparent quantum yields of ∼0.5%. This large increase can likely be attributed to more effective charge delocalization as a result of a greater density of Sn(II) $5s^2$ states with Sn(II) substitution. Upon excitation, photogenerated holes undergo rapid thermalization to the top of the valence band, i.e., the Sn(II)-based states. When there is only a small amount of Sn(II) cations, there is a higher probability for the holes to become trapped in localized Sn(II) states, leading to higher charge recombination rates. With higher amounts of Sn(II) substitution, the holes are more delocalized and have a greater probability of reaching the particles' surfaces for the water oxidation reaction.

A similar reasoning can be used to account for the differences in the visible-light only activities between the 10% and the 30% and 50% Sn(II) compositions. One alternative is that an increase in the amount of Sn(II) states at the valence band edge leads to stronger visible-light absorption. However, the slopes of their absorption edges in the diffuse reflectance data are very similar for all three compositions. The increasing substitution of Sn(II) does not appear to significantly alter the absorption coefficient and is thus unlikely to be impacting the visible-light activity. Finally, while the ultimate synthetic objective was to synthesize and investigate the fully Sn(II)-exchanged $Sn_5Nb_4O_{15}$ composition, it is likely that the 50% Sn(II) composition is sufficient to nearly reach the maximum achievable photocatalytic rates. The band gaps and photocatalytic activities of the 30% and 50% Sn(II) compositions are practically the same, indicative of reaching a “saturation point” whereby the synthesis of higher Sn(II) amounts does not yield any statistically significant change in the photocatalytic activity.

Additional photocatalytic reactions for O_2 production were tested using $Na_2S_2O_8$ as an alternate sacrificial oxidant, at concentrations of 0.05 M and 0.2 M, as has been reported previously.[45] These rates were similar or smaller to those obtained using $AgNO_3$. While the use of $Na_2S_2O_8$ avoids the deposition of Ag onto the particles' surfaces, higher rates for water oxidation were not observed. Photocatalytic tests using a Pt surface cocatalyst for H_2 production in a 20% methanol solution, as reproduced from prior reports on other Sn(II) niobates,[46] did not show any detectable activity. Further investigations of optimal surface cocatalysts and photocatalytic conditions could potentially lead to significantly higher activities. Continued research efforts toward understanding the synthesis of metastable phases such as $Sn_5Nb_4O_{15}$ are also required, such as to determine the impact of Sn(II) cations on the many known layered perovskite photocatalysts.

IV. CONCLUSIONS

Reactions of the (111) perovskite-type layered $Ba_5Nb_4O_{15}$ with a SnClF flux were used to successfully exchange Ba for Sn(II) cations, forming the metastable $(Ba_{1-x}Sn_x)_5Nb_4O_{15}$ solid solution, with x reaching up to 0.5, i.e., 50% Sn(II) cations. Attempts to exchange greater amounts of Sn(II) led to decomposition to the more thermodynamically stable constituent oxides. Total energy calculations revealed that the $(Ba_{1-x}Sn_x)_5Nb_4O_{15}$ solid solution is metastable with respect to both its simpler constituent oxides, SnO, $SnNb_2O_6$, and Nb_2O_5, but also to the lower-energy $Sn_2Nb_2O_7$. Despite the increasing metastability, the low reaction temperature helps to hinder the requisite ion diffusion required for decomposition to occur and allows for the metastable $(Ba_{1-x}Sn_x)_5Nb_4O_{15}$ compositions to be kinetically trapped. Rietveld refinement of neutron diffraction data shows that the Sn(II) cations were preferentially exchanged on the asymmetric coordination sites that were better able to accommodate the stereoactive lone pair of the Sn(II) cation. The exchange of Sn(II) cations was found to successfully red-shift the band gap from ∼3.78 eV in $Ba_5Nb_4O_{15}$ to ∼2.35 eV for $x = 0.5$. Electronic structure calculations show that the substitution of Sn(II) cations results in new higher-energy Sn $5s^2$ states at the top of the valence band, which significantly decreases its band gap. As a result, $(Ba_{1-x}Sn_x)_5Nb_4O_{15}$ is active under visible-light irradiation for photocatalytic production of O_2 without the requirement of any surface cocatalysts. The increasingly Sn(II)-exchanged compositions showed the highest photocatalytic rates for O_2 production. Thus, a new synthetic strategy is revealed that leads to the accommodation of Sn(II) cations within layered oxides, i.e., for kinetically trapping these types of metastable oxides, and which show great potential for utilization as visible-light photocatalysts for water splitting-type reactions.

■ ASSOCIATED CONTENT

Supporting Information

The Supporting Information is available free of charge at https://pubs.acs.org/doi/10.1021/acs.inorgchem.1c03846.

Powder X-ray diffraction data for reactions loaded with increasing amounts of $SnCl_2/SnF_2$, SEM imaging and elemental mapping, elemental analysis results of EDS, electron density contour plot of the conduction band states, and selected Rietveld refinement parameters and atomic coordinates (PDF)

■ AUTHOR INFORMATION

Corresponding Author

Paul A. Maggard − *Department of Chemistry, North Carolina State University, Raleigh, North Carolina 27695-8204,*

United States; orcid.org/0000-0002-3909-1590;
Email: Paul_Maggard@ncsu.edu

Authors

Shaun O'Donnell − *Department of Chemistry, North Carolina State University, Raleigh, North Carolina 27695-8204, United States*

Avery Smith − *Department of Chemistry, North Carolina State University, Raleigh, North Carolina 27695-8204, United States*

Abigail Carbone − *Department of Chemistry, North Carolina State University, Raleigh, North Carolina 27695-8204, United States*

Complete contact information is available at:
https://pubs.acs.org/10.1021/acs.inorgchem.1c03846

Notes

The authors declare no competing financial interest.

■ ACKNOWLEDGMENTS

The authors acknowledge support of this work by the National Science Foundation (DMR-2004455). A portion of this research used resources of the Advanced Photon Source, a U.S. Department of Energy (DOE) Office of Science User Facility operated for the DOE Office of Science by Argonne National Laboratory under Contract DE-AC02-06CH11357.

■ REFERENCES

(1) Wang, Q.; Domen, K. Particulate Photocatalysts for Light-Driven Water Splitting: Mechanisms, Challenges, and Design Strategies. *Chem. Rev.* **2020**, *120*, 919−985.

(2) Li, J.; Wu, N. Semiconductor-Based Photocatalysts and Photoelectrochemical Cells for Solar Fuel Generation: A Review. *Catal. Sci. Technol.* **2015**, *5*, 1360−1384.

(3) Kudo, A.; Yugo, M. Heterogeneous Photocatalyst Materials for Water Splitting. *Chem. Soc. Rev.* **2009**, *38*, 253−278.

(4) Rajeshwar, K.; Maggard, P. A.; O'Donnell, S. Semiconductor/Liquid Interface for Solar Water Splitting. *Electrochem. Soc. Interface* **2021**, *30*, 47−51.

(5) Domen, K.; Kondo, J. N.; Hara, M.; Takata, T. Photo- and Mechano-Catalytic Overall Water Splitting Reactions to Form Hydrogen and Oxygen on Heterogeneous Catalysts. *Bull. Chem. Soc. Jpn.* **2000**, *73*, 1307−1331.

(6) Maeda, K.; Mallouk, T. E. Two-Dimensional Metal Oxide Nanosheets as Building Blocks for Artificial Photosynthetic Assemblies. *Bull. Chem. Soc. Jpn.* **2019**, *92*, 38−54.

(7) Machida, M.; Yabunaka, J.; Kijima, T. Synthesis and Photocatalytic Property of Layered Perovskite Tantalates, $RbLnTa_2O_7$ (Ln = La, Pr, Nd, and Sm). *Chem. Mater.* **2000**, *12*, 812−817.

(8) Kudo, A.; Kato, H.; Nakagawa, S. Water Splitting into H_2 and O_2 on New $Sr_2M_2O_7$ (M = Nb and Ta) Photocatalysts with Layered Perovskite Structures: Factors Affecting the Photocatalytic Activity. *J. Phys. Chem. B* **2000**, *104*, 571−575.

(9) Hwang, D. W.; Kim, H. G.; Kim, J.; Cha, K. Y.; Kim, Y. G.; Lee, J. S. Photocatalytic Water Splitting over Highly Donor-Doped (110) Layered Perovskites. *J. Catal.* **2000**, *193*, 40−48.

(10) Arney, D.; Porter, B.; Greve, B.; Maggard, P. A. New Molten-Salt Synthesis and Photocatalytic Properties of $La_2Ti_2O_7$ Particles. *J. Photochem. Photobiol., A* **2008**, *199*, 230−235.

(11) Miseki, Y.; Kato, H.; Kudo, A. Water Splitting into H_2 and O_2 over $Ba_5Nb_4O_{15}$ Photocatalysts with Layered Perovskite Structure Prepared by Polymerizable Complex Method. *Chem. Lett.* **2006**, *35*, 1052−1053.

(12) Miseki, Y.; Kato, H.; Kudo, A. Water Splitting into H_2 and O_2 Over Niobate and Titanate Photocatalysts with (111) Plane-Type Layered Perovskite Structure. *Energy Environ. Sci.* **2009**, *2*, 306−314.

(13) Park, S.; Song, H. J.; Lee, C. W.; Hwang, S. W.; Cho, I. S. Enhanced Photocatalytic Activity of Ultrathin $Ba_5Nb_4O_{15}$ Two-Dimensional Nanosheets. *ACS Appl. Mater. Interfaces* **2015**, *7*, 21860−21867.

(14) Youngblood, W. J.; Anna Lee, S.-H.; Maeda, K.; Mallouk, T. E. Visible Light Water Splitting Using Dye-Sensitized Oxide Semiconductors. *Acc. Chem. Res.* **2009**, *42*, 1966−1973.

(15) Hojo, K.; Nishioka, S.; Miseki, Y.; Kamakura, Y.; Oshima, T.; Sayama, K.; Mallouk, T. E.; Maeda, K. An Improved Z-Scheme for Overall Water Splitting using Dye-Sensitized Calcium Niobate Nanosheets Synthesized by a Flux Method. *ACS Appl. Energy Mater.* **2021**, *4*, 10145−10152.

(16) Boltersdorf, J.; King, N.; Maggard, P. A. Flux-Mediated Crystal Growth of Metal Oxides: Synthetic Tunability of Particle Morphologies, Sizes, and Surface Features for Photocatalysis Research. *CrystEngComm* **2015**, *17*, 2225−2241.

(17) Arney, D.; Maggard, P. A. Effect of Platelet-Shaped Surfaces and Silver-Cation Exchange on the Photocatalytic Hydrogen Production of $RbLaNb_2O_7$. *ACS Catal.* **2012**, *2*, 1711−1717.

(18) Boltersdorf, J.; Maggard, P. A. Silver Exchange of Layered Metal Oxides and Their Photocatalytic Activities. *ACS Catal.* **2013**, *3*, 2547−2555.

(19) Watanabe, K.; Iwashina, K.; Iwase, A.; Nozawa, S.; Adachi, S.-i.; Kudo, A. New Visible-Light-Driven H_2- and O_2-Evolving Photocatalysts Developed by Ag(I) and Cu(I) Ion Exchange of Various Layered and Tunneling Metal Oxides Using Molten Salts Treatments. *Chem. Mater.* **2020**, *32*, 10524−10537.

(20) Noureldine, D.; Takanabe, K. State-of-the-Art Sn^{2+}-Based Ternary Oxides as Photocatalysts for Water Splitting: Electronic Structures and Optoelectronic Properties. *Catal. Sci. Technol.* **2016**, *6*, 7656−7670.

(21) Noureldine, D.; Anjum, D. H.; Takanabe, K. Flux-Assisted Synthesis of $SnNb_2O_6$ for Tuning Photocatalytic Properties. *Phys. Chem. Chem. Phys.* **2014**, *16*, 10762−10769.

(22) Cho, I.-S.; Kwak, C. H.; Kim, D. W.; Lee, S.; Hong, K. S. Photophysical, Photoelectrochemical, and Photocatalytic Properties of Novel $SnWO_4$ Oxide Semiconductors with Narrow Band Gaps. *J. Phys. Chem. C* **2009**, *113*, 10647−10653.

(23) Zou, Y.; Le, J.; Cao, Y.; An, N.; Zhou, Y.; Li, J.; Liu, D.; Kuang, Y. Tetragonal Tungsten Bronze Type Sn(II)-Based Quaternary Oxides: A New Class of Visible-Light-Absorbing Semiconductors for Photoelectrochemical Water Oxidation. *J. Mater. Chem. A* **2021**, *9*, 21085−21093.

(24) O'Donnell, S.; Hamilton, A.; Maggard, P. A. Fast Flux Reaction Approach for the Preparation of Sn_2TiO_4: Tuning Particles Sizes and Photocatalytic Properties. *J. Electrochem. Soc.* **2019**, *166*, H3084−H3090.

(25) Boltersdorf, J.; Sullivan, I.; Shelton, T.; Wu, Z.; Gray, M.; Zoellner, B.; Osterloh, F.; Maggard, P. A. Flux Synthesis, Optical and Photocatalytic Properties of n-Type Sn_2TiO_4: Hydrogen and Oxygen Evolution under Visible Light. *Chem. Mater.* **2016**, *28*, 8876−8889.

(26) Giefers, H.; Porsch, F.; Wortmann, G. Kinetics of the Disproportionation of SnO. *Solid State Ionics* **2005**, *176*, 199−207.

(27) Moreno, M. S.; Punte, G.; Rigotti, G.; Mercader, R. C.; Weisz, A. D.; Blesa, M. A. Kinetic Study of the Disproportionation of Tin Monoxide. *Solid State Ionics* **2001**, *144*, 81−86.

(28) O'Donnell, S. C.; Chung, C. C.; Carbone, A.; Broughton, R.; Jones, J. L.; Maggard, P. A. Pushing the Limits of Metastability in Semiconducting Perovskite Oxides for Visible-Light-Driven Water Oxidation. *Chem. Mater.* **2020**, *32*, 3054−3064.

(29) Gabilondo, E. A.; O'Donnell, S.; Broughton, R.; Jones, J. L.; Maggard, P. A. Synthesis and Stability of Sn(II)-Containing Perovskites: $(Ba,Sn^{II})Hf^{IV}O_3$ versus $(Ba,Sn^{II})Sn^{IV}O_3$. *J. Solid State Chem.* **2021**, *302*, No. 122419.

(30) Maggard, P. A. Capturing Metastable Oxide Semiconductors for Applications in Solar Energy Conversion. *Acc. Chem. Res.* **2021**, *54*, 3160−3171.

(31) Toby, B. H.; Von Dreele, R. B. GSAS-II: The Genesis of a Modern Open-Source All Purpose Crystallography Software Package. *J. Appl. Crystallogr.* **2013**, *46*, 544−549.

(32) Weckhuysen, B. M.; Schoonheydt, R. A. Recent Progress in Diffuse Reflectance Spectroscopy of Supported Metal Oxide Catalysts. *Catal. Today* **1999**, *49*, 441−451.

(33) McLamb, N.; Sahoo, P. P.; Fuoco, L.; Maggard, P. A. Flux Growth of Single-Crystal $Na_2Ta_4O_{11}$ Particles and Their Photocatalytic Hydrogen Production. *Cryst. Growth Des.* **2013**, *13*, 2322−2326.

(34) Hamilton, A.; O'Donnell, S. C.; Zoellner, B.; Sullivan, I.; Maggard, P. A. Flux-Mediated Synthesis and Photocatalytic Activity of $NaNbO_3$ Particles. *J. Am. Ceram. Soc.* **2020**, *103*, 454−464.

(35) Kresse, G.; Hafner, J. Efficiency of Ab Initio Total Energy Calculations for Metals and Semiconductors Using a Plane-Wave Basis Set. *Comput. Mater. Sci.* **1996**, *6*, 15−50.

(36) Kresse, G.; Furthmuller, J. Efficient Iterative Schemes for Ab Initio Total-Energy Calculations Using a Plane-Wave basis Set. *Phys. Rev. B* **1996**, *54*, 11169−11186.

(37) Perdew, J. P.; Burke, L.; Ernzerhof, M. Generalized Gradient Approximation Made Simple. *Phys. Rev. Lett.* **1996**, *77*, 3865−3868.

(38) Hautier, G.; Ong, S. P.; Jain, A.; Moore, C. J.; Ceder, G. Accuracy of Density Functional Theory in Predicting Formation Energies of Ternary Oxides from Binary Oxides and its Implication on Phase Stability. *Phys. Rev. B* **2012**, *85*, No. 155208.

(39) Benisek, A.; Dachs, E. The Accuracy of Standard Enthalpies and Entropies for Phases of Petrological Interest Derived from Density-Functional Calculations. *Contrib. Mineral. Petrol.* **2018**, *173*, No. 90.

(40) Kirklin, S.; Saal, J. E.; Meredig, B.; Thompson, A.; Doak, J. W.; Aykol, M.; Ruhl, S.; Wolverton, C. The Open Quantum Materials Database (OQMD): Assessing the Accuracy of DFT Formation Energies. *npj Comput. Mater.* **2015**, *1*, No. 15010.

(41) Walsh, A.; Payne, D. J.; Egdell, R. G.; Watson, G. W. Stereochemistry of Post-Transition Metal Oxides: Revision of the Classical Lone Pair Model. *Chem. Soc. Rev.* **2011**, *40*, 4455−4463.

(42) Vanderah, T. A.; Collins, T. R.; Wong-Ng, W.; Roth, R. S.; Farber, L. Phase Equilibria and Crystal Chemistry in the $BaO-Al_2O_3-Nb_2O_5$ and $BaO-Nb_2O_5$ Systems. *J. Alloys Compd.* **2002**, *346*, 116−128.

(43) Taira, N.; Kakinuma, T. Photocatalytic Activity of $Sn_2M_2O_7$ (M = Nb and Ta) Pyrochlore Oxides with Blue LEDs Irradiation. *J. Ceram. Soc. Jpn.* **2012**, *120*, 551−553.

(44) Diehl, L.; Fabini, D. H.; Vargas-Barbosa, N. M.; Jiménez-Solano, A.; Block, T.; Duppel, V.; Moudrakovski, I.; Küster, K.; Pöttgen, R.; Lotsch, B. V. Interplay between Valence Band Tuning and Redox Stability in $SnTiO_3$: Implications for Directed Design of Photocatalysts. *Chem. Mater.* **2021**, *33*, 2824−2836.

(45) Schneider, J.; Bahnemann, D. W. Undesired Role of Sacrificial Reagents in Photocatalysis. *J. Phys. Chem. Lett.* **2013**, *4*, 3479−3483.

(46) Seo, S. W.; Noh, T. H.; Park, S.; Lee, C. W.; Kim, S. H.; Kim, H. J.; Park, H. K.; Hong, K. S. Solvothermal synthesis of $SnNb_2O_6$ nanoplates and enhanced photocatalytic H_2 evolution under visible light. *Int. J. Hydrogen Energy* **2014**, *39*, 17517−17523.